encit 2020

ABCM
Associação Brasileira de Engenharia e Ciências Mecânicas

18th Brazilian Congress of Thermal Sciences and Engineering
November 16–20, 2020, (Online)

ENC-2020-0181
Assessment of Galerkin and Least-Squares Petrov-Galerkin reduced-order models for unsteady flows

Victor Zucatti da Silva
William R. Wolf
University of Campinas, Campinas, SP, 13083-860, Brazil
victor.zucatti@gmail.com, wolf@fem.unicamp.br

Abstract. *An assessment of physics-based reduced-order models (ROMs) is presented for the study of unsteady flows. Here, we preliminary tests are conducted for analysis of convective heat transfer in a rectangular cavity. Despite the simple geometrical configuration, the current setup offers increasingly rich dynamics as the thermal forcing is increased, thus making it a suitable candidate to evaluate the performance of ROMs. First, flow simulations are performed using a high-order spectral element method that will feed the ROMs with well-resolved temporal and spatial information. Then, proper orthogonal decomposition (POD) is applied to reduce the problem dimensionality for all models. The class of tested physics-based models include the Galerkin and least-squares Petrov-Galerkin (LSPG) methods that rely on projection of the Navier-Stokes and energy equations being solved. All ROMs are able to represent the chaotic temporal dynamics of a moderate Rayleigh number flow. .*

Keywords: *Reduced order modeling, proper orthogonal decomposition, Galerkin projection.*

1. INTRODUCTION

The development of reduced-order models (ROMs) for solving partial differential equations has received considerable attention in the past decade Carlberg *et al.* (2017); Bergmann *et al.* (2018); Amsallem *et al.* (2012). Studies of convective heat transfer can benefit from ROMs including applications in preliminary design, optimization and flow & thermal control. In general, the solution of the full-order model (FOM) via discretization of the coupled Navier-Stokes and energy equations requires intense computational power. For such cases, the solution of unsteady flows is typically obtained by high-order, low-dissipation, numerical schemes that can accurately capture the dynamically important temporal and spatial scales of the flow. Full-order numerical procedures are often solved in parallel computers and are associated with high simulation costs.

In order to be applied to problems involving unsteady flows, ROMs should be accurate and represent the main physical mechanisms computed by FOMs. Moreover, they should be stable for long-term temporal integration to allow calculation of meaningfully converged statistics. Despite all advances in the field, application of ROMs to complex unsteady flows is still a challenging task. Several methods have been proposed in the literature and those based on projection of the Navier-Stokes equations are the most popular. Among these techniques, we mention Galerkin (Rowley *et al.*, 2004) and least-squares Petrov-Galerkin (LSPG) projections (Carlberg *et al.*, 2013; A Quarteroni and Negri, 2016). Both methodologies are directly related to the problem physics through projection of the partial differential equations into sets of ordinary differential equations. The projection is usually performed using orthogonal functions computed via proper orthogonal decomposition (POD) Sirovich (1987); Cordier and Bergmann (2008).

Galerkin and LSPG projections require the discretization of linear and non-linear spatial operators appearing in the FOM, what may still imply high simulation costs. Moreover, in some cases, ROMs constructed using Galerkin projection may exhibit unstable behavior (Carlberg *et al.*, 2013) due to the inherent basis truncation occurring in this method. In turbulent flows, basis truncation removes higher POD modes from the flow reconstruction, which results in an unbalance of turbulent kinetic energy budget of the ROM. This occurs because the absent modes are mostly associated to small dissipative scales which would prevent amplification of numerical instabilities. This issue may be addressed by application of turbulence models (Cazemier *et al.*, 1998; Östh *et al.*, 2014; Protas *et al.*, 2015) but this approach can compromise consistency between the original partial differential equations and the ROM. Other alternatives have been proposed to deal with this problem via minimal rotation of the projected subspace (Balajewicz *et al.*, 2016). Recently, San and Maulik San and Maulik (2018a) employed neural networks to compute optimal coefficients for an eddy viscosity model which is able to stabilize a Galerkin projection ROM. Another issue with Galerkin and LSPG methods is related to inherent high costs from solving problems with strong non-linearities, an issue that can be dealt with by application of hyper-reduction techniques (Chaturantabut and Sorensen, 2010; Zimmermann and Willcox, 2016; Willcox, 2006).

In the present extended abstract we employ the POD-Galerkin and LSPG techniques to study convective heat transfer in a rectangular cavity. Despite the simple geometrical configuration, the current setup offers increasingly rich dynamics as the thermal forcing is increased, thus making it a suitable candidate to evaluate the performance of ROMs. Aspects of spatial discretization and hyper-reduction are addressed. In the final version of the paper, further aspects of cluster-basis POD will be discussed including higher Rayleigh number flows.

2. Problem description

The reduced-order modeling approaches considered in this study are applied to the problem of a two-dimensional differentially heated rectangular cavity of aspect ratio $A \equiv H/W = 8.0$, where H and W denote the height and width of the cavity, respectively. As shown in Fig. 1(a), the horizontal walls are adiabatic and fluid is heated from the left and cooled from the right-hand side. The presence of a gravitational force in the negative vertical direction induces a buoyant force which causes hot and cold fluid to move upward and downward, respectively. Despite its geometrical simplicity, this setup offers increasingly rich dynamics as the thermal forcing is increased, thus making it a suitable candidate to evaluate the performance of ROMs.

The particular choice for the aspect ratio, $A = 8.0$, is motivated by the availability of benchmark data (e.g. refs. Christon *et al.* (2002); Xin and Quere (2002); Gjesdal *et al.* (2006)) and by a recent study San and Maulik (2018b) that utilized the same setup to evaluate the performance of machine learning closures on stabilization of a projection-based ROM. For $Ra = 5.5 \times 10^5$, Fig. 1(b) suggests the existence of finer scale structures which increase the number of POD modes necessary to construct a suitable basis, thus increasing the complexity of reduced-order models. Additionally, the flow dynamics are non-periodic for this higher value of Rayleigh number, which represents a challenge for construction of accurate and stable ROMs.

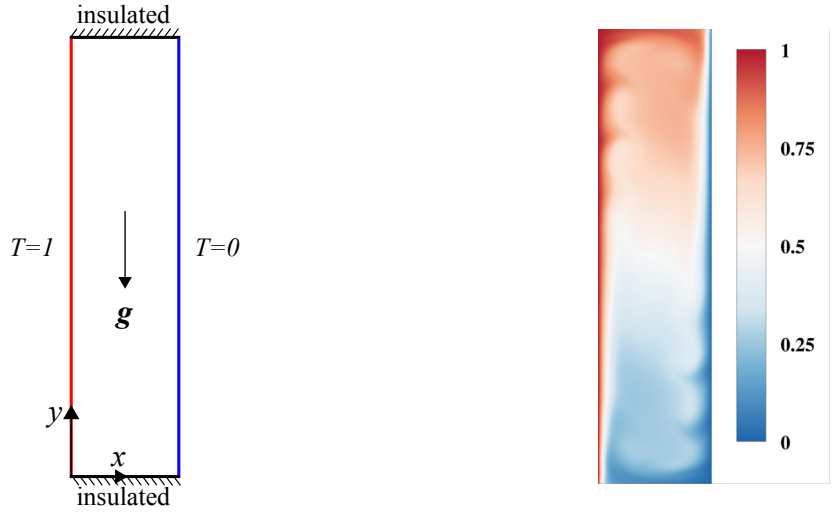

Figure 1: Geometry and thermal boundary conditions for a differentially heated cavity of height H, width W, and aspect ratio $A = H/W = 8$ (left). Representative instantaneous temperature contour for $Ra = 5.5 \times 10^5$ (right).

2.1 Governing equations

The flow is governed by the continuity, momentum and energy equations in incompressible form. Density variations with temperature are accounted for using the Boussinesq approximation. In non-dimensional form, these equations are given by

$$\nabla \cdot \mathbf{u} = 0 \,, \tag{1}$$

$$\frac{\partial \mathbf{u}}{\partial t} + \mathbf{u} \cdot \nabla \mathbf{u} = -\nabla p + \sqrt{\frac{Pr}{Ra}} \nabla^2 \mathbf{u} + T\mathbf{j} \,, \tag{2}$$

and

$$\frac{\partial T}{\partial t} + \mathbf{u} \cdot \nabla T = \frac{1}{\sqrt{RaPr}} \nabla^2 T \,. \tag{3}$$

In these equations, $\mathbf{u} = (u, v)$ represents the velocity vector, p is the reduced pressure, and T is the temperature. The cavity width W is used as a reference length scale, while $\mathbf{u}$ is normalized by the free-fall velocity $U = \sqrt{g\beta\Delta T W}$, and

$\tau = W/U$ is used as a time scale. The temperature difference is $\Delta T = T_H - T_C$, with T_H and T_C denoting the hot and cold temperatures, respectively. The non-dimensional temperature is $T = (T^* - T_C)/\Delta T$, where T^* is the dimensional temperature. The gravitational acceleration is g, and β is the thermal expansion coefficient.

The flow is governed by two non-dimensional parameters, the Prandtl and Rayleigh numbers given by

$$Pr = \frac{\nu}{\alpha} \tag{4}$$

and

$$Ra = \frac{g\beta\Delta T W^3}{\nu\alpha}\ , \tag{5}$$

respectively, where ν is the kinematic viscosity and α is the thermal diffusivity. Here, we use $Pr = 0.71$, which is representative of air. The Rayleigh number is set as $Ra = 5.5 \times 10^5$. A no-slip boundary condition is used on the walls, and temperature is set as $T = 1$ on $x = 0$, $T = 0$ on $x = 1$, and $\partial T/\partial y = 0$ on the horizontal walls, where x is the horizontal coordinate normalized by the cavity width.

2.2 Numerical method for full-order model

The governing equations are discretized in dimensional form using quadrilateral spectral elements on a two-dimensional plane, using the formulation described by Blackburn & Sherwin Blackburn and Sherwin (2004). In a spectral element framework, the expansion bases and test functions used in the Galerkin method consist of high-order polynomials which provide spectral convergence for smooth solutions as the polynomial order is increased. Here, we use a nodal spectral element formulation where Lagrange polynomials are interpolated on a set of nodal points, which in the present formulation consists of the Gauss-Lobatto-Legendre (GLL) nodes.

Time-integration is carried out using the second-order, stiffly stable velocity correction scheme described by Karniadakis et al. Karniadakis *et al.* (1991). The scheme is semi-implicit so that non-linear terms are computed explicitly, while viscous terms are solved implicitly, forming a Helmholtz equation. Thus, the time step size used in the simulations is limited by a CFL-like condition. For further details about the numerical method employed for the FOM the reader may consult refs. Blackburn and Sherwin (2004); Karniadakis *et al.* (1991); Karniadakis and Sherwin (2013).

2.3 Comparison with benchmark data

The domain shown in Fig. 1(a) is discretized using 800 spectral elements, with 80 and 10 elements in the y and x directions, respectively, which are constructed using polynomials of order $P = 10$, thus giving approximately $80,000$ independent degrees of freedom. To ensure the quality of the solutions obtained on this mesh, results for $Ra = 3.4 \times 10^5$ are compared with benchmark data provided in refs. Christon *et al.* (2002); Xin and Quere (2002), as shown in table 1. In the table, $\overline{u}$ and $\overline{T}$ denote the time-averaged values obtained for the horizontal velocity and for the temperature at the point $(x, y) = (0.181, 7.37)$, while u' and T' represent their respective fluctuations. The global Nusselt number Nu is obtained from

$$Nu = \frac{1}{H}\frac{W}{\Delta T}\int_0^H \left.\frac{\partial T}{\partial x}\right|_{x=0} dy, \tag{6}$$

so that it is the area-averaged ratio of convective and conductive heat transfer on the hot wall. From the results shown in the table, it is clear that all quantities are in excellent agreement with the benchmark data. Note that in the present study we consider a higher Rayleigh number of $Ra = 5.5 \times 10^5$ since the dynamics for such flow is more complex than that for $Ra = 3.4 \times 10^5$. While the latter depicts periodical fluctuations, the former presents a more chaotic behavior, leading to a more challenging problem for application of ROMs. To ensure that the grid with 800 elements is adequate for the higher Ra, a simulation was performed with $Ra = 5.5 \times 10^5$ on this mesh and also on a finer grid with 1600 elements and $P = 10$. Time-averaged first-and second-order statistics revealed that differences in the numerical results obtained on the two meshes were negligible. Thus, all the FOM simulations reported throughout the paper were obtained on the mesh with 800 spectral elements.

As explained later, snapshots are collected from solutions obtained from the FOM and provided as inputs to the ROMs. Before this, however, a spatial interpolation is performed from the spectral element mesh described above onto a grid with spatial distributions such that the grid spacing increases monotonically from the cavity walls toward the cavity centre. Note that, in the case of a spectral element mesh, inner grid points are always clustered near element boundaries, which would not provide a favorable distribution for using finite-difference spatial differential schemes, as done in the present work for the Galerkin and LSPG methods. Hence, an interpolated grid consisting of $84\,234$ grid points has been employed for the snapshots, although both solutions are obtained in the FOM on a grid with 800 spectral elements with $P = 10$.

Table 1: Time-averaged and respective fluctuations of horizontal velocity, temperature and global Nusselt number at $(x, y) = (0.181, 7.37)$. τ_θ denotes the period of one oscillation.

	$\overline{u}$	u'	$\overline{T}$	T'	$\overline{Nu}$	Nu'	τ_θ
Present results	0.056341	0.054766	0.765475	0.042689	4.57946	0.007087	3.41505
Christon *et al.* (2002); Xin and Quere (2002)	0.056356	0.054828	0.765480	0.042740	4.57946	0.007100	3.41150

3. Proper orthogonal decomposition

In proper orthogonal decomposition, unsteady velocity and temperature fields can be decomposed as follows

$$\mathbf{q}(\mathbf{x}, t) = \bar{\mathbf{q}}(\mathbf{x}) + \sum_{i=1}^{N} \mathbf{\Phi_i}(\mathbf{x})\mathbf{a_i}(\mathbf{t}) \,, \tag{7}$$

where $\mathbf{q} = \{u, v, T\}^\top$, $\mathbf{\Phi_i}$ are the orthonormal spatial eigenfunctions, $\mathbf{a_i}$ represent the temporal modes and $\{\cdot\}^\top$ is the transpose of $\{\cdot\}$. N is the number of data sets extracted from the numerical simulation and i represents the mode index. Reconstruction of the fluctuation velocity and temperature fields can then be approximated by

$$\mathbf{q}'(\mathbf{x}, t) \approx \sum_{i=1}^{M} \mathbf{\Phi_i}(\mathbf{x})\mathbf{a_i}(\mathbf{t}) \,, \tag{8}$$

where M is the number of modes used in the fluctuation field reconstruction. In practical ROM applications, one seeks $M \ll N$.

In the POD it is usually necessary to calculate a covariance matrix $\mathbf{C}$ given by

$$C_{i,j} = \frac{1}{N} \int_\Omega q_i(\mathbf{x}, t_i)\, q_j(\mathbf{x}, t_j)\, d\mathbf{x} \,. \tag{9}$$

This matrix is symmetric positive semidefinite and, therefore, allows the use of singular value decomposition to compute the singular values and vectors of the POD reconstruction. From this matrix factorization we have the calculation of the orthonormal spatial eigenfunctions that will be used in the Galerkin and LSPG projections to reconstruct the system of ordinary differential equations that, in turn, will determine the evolution of temporal modes. Such modes are calculated so that the reconstruction is optimal in the sense of truncated mean quadratic error.

The idea of writing a temporal covariance matrix comes from the fact that solution cost grows rapidly for large computational grids. This is an issue especially in multidimensional problems. This alternative technique used to obtain a POD modal basis is referred to as snapshot method and was introduced in Sirovich (1987). It consists of solving a much smaller eigenvalue problem proportional to the time complexity (number of snapshots) written as

$$\mathbf{C}\xi_\mathbf{j} = \mathbf{X^T X}\xi_\mathbf{j} = \lambda_j \xi_\mathbf{j}, \quad \xi_\mathbf{j} \in \mathbb{R}^N, \quad N \ll N_g \,, \tag{10}$$

where $\mathbf{X^T X}$ is of dimension $N \times N$. Here, N_g refers to the total number of grid points. Spatial eigenfunctions $\mathbf{\Phi}$ are then recovered using the temporal modes $\mathbf{\Xi}$ obtained through the reduced eigenvalue problem

$$\mathbf{\Phi} = \mathbf{X\Xi\Lambda}^{-1/2} \tag{11}$$

where $\mathbf{\Phi} = [\Phi_1\ \Phi_2\ \ldots\ \Phi_N] \in \mathbb{R}^{N_g \times N}$ and $\mathbf{\Xi} = [\xi_1\ \xi_2\ \ldots\ \xi_N] \in \mathbb{R}^{N \times N}$. This method is widely applied due to its reduced computational effort and memory usage.

4. Projection Methods

Consider a dynamical system $\mathbf{F}(\mathbf{q})$ defined in a connected open region $\Omega \subset \mathbb{R}^{N_g}$ whose boundary Γ is well defined

$$\begin{cases} \mathbf{F}(\mathbf{q}) = \frac{d\mathbf{q}}{dt} - \mathbf{G}(\mathbf{q}) = \mathbf{0} \quad in \quad \Omega \\ \mathbf{q}(t=0) = \mathbf{u_0} \\ \mathbf{q} = \mathbf{g} \quad on \quad \Gamma \,, \end{cases} \tag{12}$$

where $\mathbf{q}$ is a function of space and time, and the nonlinear operator $\mathbf{G}(\mathbf{q})$ is given by the convective and diffusive terms appearing in the momentum and energy equations. Let $\mathbf{\Phi}$ define an orthonormal basis obtained by the POD method. The

state variable $\mathbf{q}$ is approximated as the linear combination of this basis vector as

$$\mathbf{q} \approx \hat{\mathbf{q}} = \bar{\mathbf{q}} + \sum_{i=1}^{M} \mathbf{\Phi_i}\, \mathbf{a_i}\ . \tag{13}$$

In this case, orthogonality of the residual $\mathbf{R}(\hat{\mathbf{q}})$ is enforced as

$$\mathbf{R}(\hat{\mathbf{q}}) = \langle \mathbf{\Psi_i}, \mathbf{F}(\hat{\mathbf{q}}) \rangle = 0\ , \tag{14}$$

where $\mathbf{\Psi_i}$ is the test space and $\langle . \rangle$ denotes the L^2 norm. A projection method is generally called Galerkin (Petrov-Galerkin) when the test and solution bases are equal (different), i.e. $\mathbf{\Phi} = \mathbf{\Psi}$ ($\mathbf{\Phi} \neq \mathbf{\Psi}$) for the following projection

$$\langle \mathbf{\Psi_i}, \mathbf{F}(\bar{\mathbf{q}} + \sum_{i=1}^{M} \mathbf{\Phi_i a_i}) \rangle = 0\ . \tag{15}$$

Boundary conditions must be implicitly satisfied by the POD solution basis, otherwise the problem may lead to an ill-conditioned or ill-posed reduced-order model. Homogeneous Dirichlet or Neumann boundary conditions can be inherited by the spatial modes $\mathbf{\Phi}$ from the snapshot collection Bergmann *et al.* (2005).

4.1 Galerkin Projection

Galerkin projection is a widely used method for reduced-order modeling of dynamical systems. This can be attributed to its implementation simplicity and mathematical robustness. Applying the Galerkin projection method to equation 12 we have

$$\langle \mathbf{\Phi_i}, \sum_{j=1}^{M} \mathbf{\Phi_j \dot{a}_j} \rangle = \langle \mathbf{\Phi_i}, \mathbf{G}(\bar{\mathbf{q}} + \sum_{j=1}^{M} \mathbf{\Phi_j a_j}) \rangle\ . \tag{16}$$

This equation can be further simplified since the functions $\mathbf{\Phi_i}$ are orthonormal. Hence, a system of ordinary differential equations arises for the temporal modes as

$$\frac{\mathrm{d}\mathbf{a_i}}{\mathrm{dt}} = \langle \mathbf{\Phi_i}, \mathbf{G}(\bar{\mathbf{q}} + \sum_{j=1}^{M} \mathbf{\Phi_j a_j}) \rangle\ , \tag{17}$$

with initial conditions obtained by projection of a single snapshot in the vector basis

$$\mathbf{a_i}(0) = \langle \mathbf{q}(\mathbf{x}, 0), \mathbf{\Phi_i}(\mathbf{x}) \rangle\ . \tag{18}$$

The previous system of ordinary differential equations represents the ROM associated to the FOM and can be integrated in time. The right-hand side of Eq. 17 should have a reduced computational cost compared to the full-order model to justify its application. Following the POD-Galerkin approach, the reduced-order model for the thermal convection problem has the form

$$\frac{d\mathbf{a}}{dt} = \mathbf{e} + \mathbf{A}\mathbf{a} + \mathbf{a}^T \mathbf{N} \mathbf{a}\ , \tag{19}$$

where the coefficients $\mathbf{e}$, $\mathbf{A}$ and $\mathbf{N}$ can be found in 6. It is worth mentioning that these coefficients are time-independent and, thus, need to be calculated only once, in a pre-processing step.

4.2 Least-Squares Petrov-Galerkin

The Least-Squares Petrov-Galerkin (LSPG) technique is presented in Carlberg *et al.* (2013, 2017); A Quarteroni and Negri (2016). The discrete test basis $\mathbf{\Psi_i}$ is given by

$$\mathbf{\Psi_i} = \mathbf{\Phi_i}^{\top} \frac{\partial \mathbf{R}(\hat{\mathbf{q}})}{\partial \mathbf{a}}\ , \tag{20}$$

which is equivalent to solving the following minimization problem

$$\underset{\hat{q} \in span(\mathbf{\Phi})}{\text{minimize}} \|\mathbf{R}(\hat{\mathbf{q}})\|_2\ . \tag{21}$$

The previous regression problem can be linear or nonlinear depending on the time integration scheme employed (explicit or implicit) and the set of equations being solved. The LSPG solution may converge to that obtained from Galerkin projection as the time step approaches zero as discussed in Carlberg *et al.* (2017). This reference also shows that the optimal time step for an implicit LSPG is given by a particular time step, depending on the problem at hand. The initial condition is also given by Eq. 18.

4.3 Hyper-Reduction

The LSPG method scales in computational cost with the FOM even though the test space is smaller than that of the full POD reconstruction. A further approximation to a much smaller problem using hyper-reduction techniques is crucial for reduction of computational costs. Hyper-reduction is also a requirement when modeling problems with strong nonlinearities (i.e. non-polynomial) or non-affine parameter dependence.

The gappy POD approximation Everson and Sirovich (1995) can be used to solve this problem by switching to low-rank "gappy modes"; within this approach, only a few grid points are used to solve the minimization problem. This method was used, for instance by Willcox (2006) for optimal sensor placement and by Carlberg *et al.* (2013) for turbulent flow modeling.

Several near-optimal node sampling procedures have been proposed in the last 20 years. The missing point estimation (MPE) method Astrid *et al.* (2008) chooses the nodes that best approximate $\langle \mathbf{\Phi_i}, \mathbf{\Phi_j} \rangle \approx \mathbf{I}$. These nodes are initially selected by condition number evaluation with a greedy algorithm of the previous near identity matrix, but computational cost may rapidly become prohibitive.

A widely used alternative to MPE is the discrete empirical interpolation method (DEIM) Chaturantabut and Sorensen (2010). This sampling procedure first appeared as a method of interpolation for reduced-order modeling of nonlinear problems. However, in the DEIM, the number of sampled nodes is limited to the number of POD modes used in the reconstruction. This is a limiting factor for problems where a large set of sampled nodes is preferable or mandatory. In the present work, nodes are sampled according to the accelerated greedy missing point estimation procedure algorithm proposed by Zimmermann and Willcox (2016). First, this method applies the DEIM and, then, an indirect condition number evaluation is performed by a greedy method to find additional nodes according to the MPE procedure.

5. Preliminary Results and Discussion

In this section the reduced-order modeling approaches presented in Section 4are evaluated in the context of convective heat transfer in a two-dimensional rectangular cavity. As discussed in Section 2.the flow condition investigated includes the thermal convection at moderate Rayleigh number $Ra = 5.5 \times 10^5$. Results obtained for the full- and reduced-order models are compared in terms of velocity and temperature fluctuations for specific probe locations. The capability of different ROMs to reproduce the POD temporal modes is also assessed. Moreover, flow snapshots of the FOM and ROMs are compared at selected time instants. Errors are reported in terms of the L_2 error norm computed for fluctuating quantities as

$$Error(t) = \frac{\|\mathbf{q'_{FOM}}(\mathbf{x},t) - \mathbf{q'_{ROM}}(\mathbf{x},t)\|_{L_2}}{\|\mathbf{q'_{FOM}}(\mathbf{x},t)\|_{L_2}} \, . \tag{22}$$

Finite difference centered schemes of different orders of accuracy are used to compute derivatives of POD spatial modes in the physics-based ROMs. The influence of resolution in these calculations is shown to be relevant for the current moderate Rayleigh number case and, therefore, will be discussed later in this section. An explicit 4^{th}-order Runge-Kutta time-marching scheme is used in both projection methods and Δt_{ROM} is selected as the time step between snapshots.

5.1 Moderate Rayleigh number case ($Ra = 5.5 \times 10^5$)

For the current flow, the temporal dynamics are irregular, composed of several frequencies, what consists in a challenge for ROMs. The simulation is recorded for $8\,000$ snapshots with a non-dimensional time step $\Delta t_{\text{snapshot}} = 1$ obtained on a fine grid with $84\,234$ nodes. The first half of the snapshots ($N = 4,000$) are used to construct a POD basis and only 40 spatial modes are retained for construction of the ROMs. These 40 modes represent 99.96% of the model energy. Solutions are presented in terms of flow and thermal fluctuations using only 14 POD modes for all ROMs. Unless indicated, all solutions presented by the LSPG approach are obtained using $8\,574$ points in the hyper-reduction technique.

Figure 5 shows the 8^{th} and 14^{th} POD temporal modes used for training and testing the ROMs. The red vertical line marks the end of the training dataset. One can see in this figure that the temporal dynamics of these modes are complex, non-periodical, composed by several Fourier modes. Both the Galerkin and LSPG methods are able to accurately reproduce the dynamics of the training window and theirs solution beyond the training dataset show good agreement.

The temporal evolution of temperature and velocity fluctuations are presented in Fig. 3. Results are computed for a probe located near the cavity top-left corner at $(x, y) = (0.181, 7.37)$. From this figure, it is possible to see that the flow dynamics are chaotic with no specific pattern for the fluctuations. Both the Galerkin and LSPG techniques are able to reproduce the FOM solution beyond the training window.

Figures 4a, 4b, 4c present snapshots of temperature, u and v-velocity fluctuations obtained at time $t = 7,600$, respectively. The snapshots allow a comparison of results between FOM and ROMs for a flow reconstruction with 14 POD modes out of $4,000$. Small discrepancies between the ROM and FOM solutions are evident, especially for small scale flow structures. However, the main features of the flow are recovered. Again, the more intense flow structures appear on

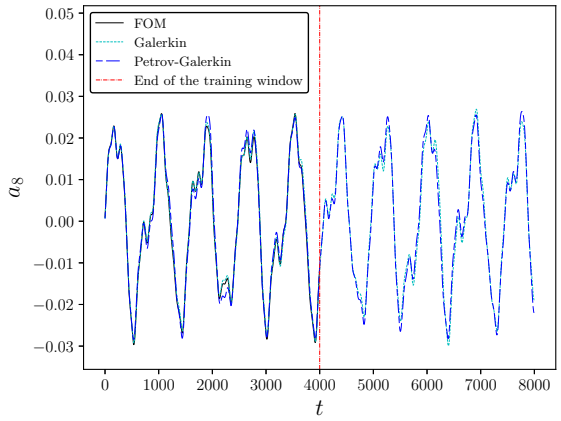

(a) Temporal mode 8.

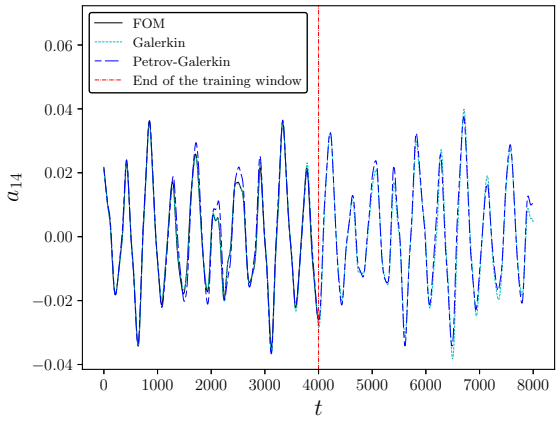

(b) Temporal mode 14.

Figure 2: Dynamics of POD temporal modes 8 and 14 for $Ra = 5.5 \times 10^5$.

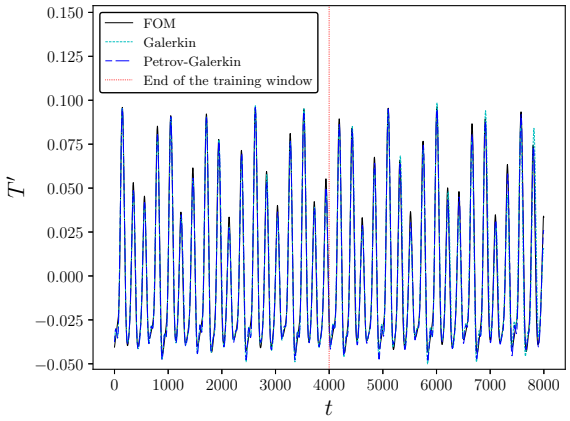

(a) Temperature.

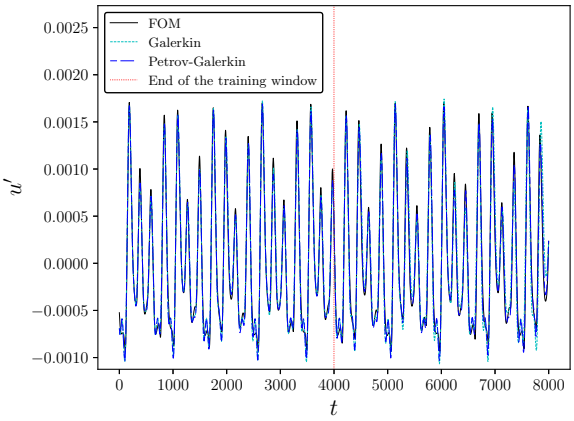

(b) u-velocity.

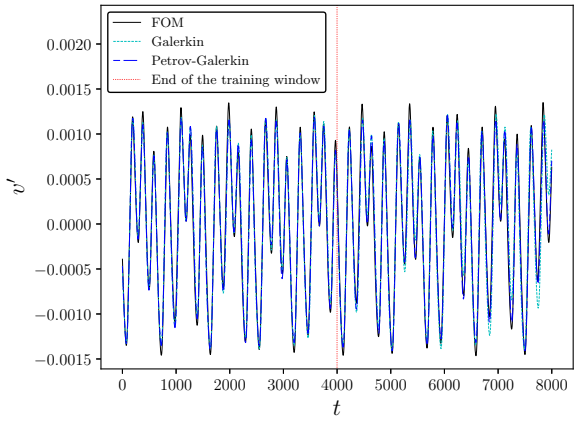

(c) v-velocity.

Figure 3: Time histories of temperature and velocity fluctuations computed by the FOM and ROMs at $(x, y) = (0.181, 7.37)$ for $Ra = 5.5 \times 10^5$.

the top-left and bottom-right corners, what justifies the previous probe location for computing the flow fluctuations. For all fluctuation fields, structures of different scales can be observed and, in general, the present physics-based models are able to reproduce most of the details of the FOM.

Both ROM approaches tested require the computation of spatial derivatives appearing in the momentum and energy

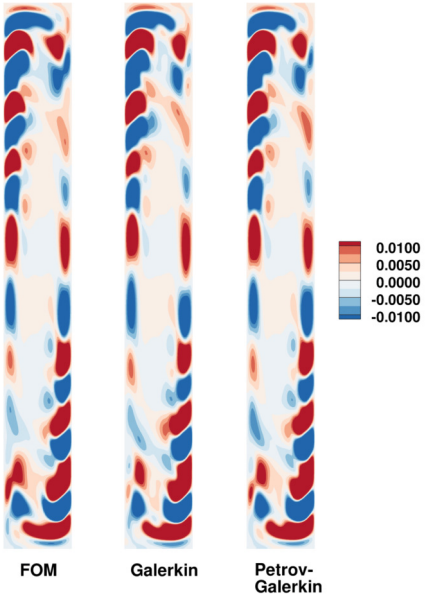

(a) Contours of temperature.

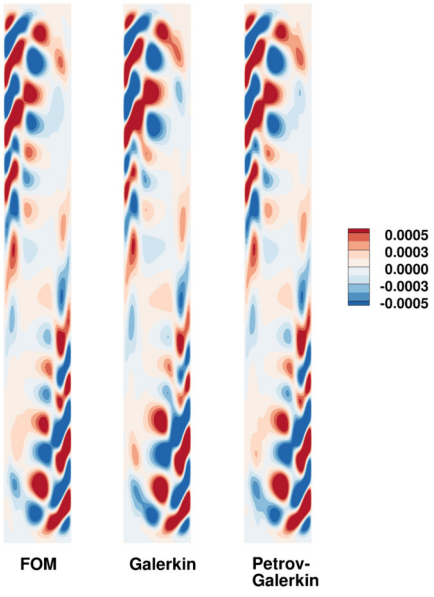

(b) Contours of v-velocity.

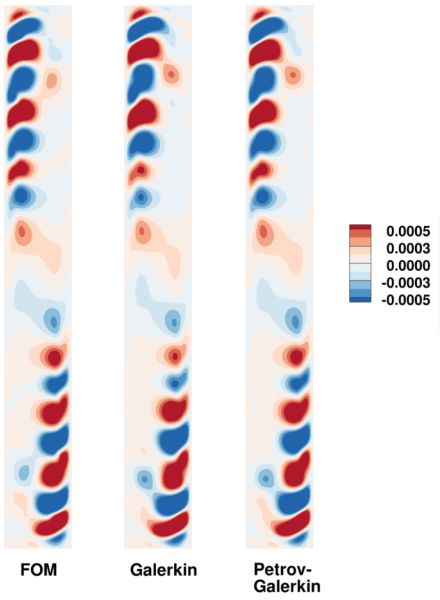

(c) Contours of u-velocity.

Figure 4: Contours at $t = 7600$ for $Ra = 5.5 \times 10^5$

equations. In this extended abstract, we also investigate the sensitivity of the Galerkin and LSPG methods to various differentiation schemes. We perform such tests on the LSPG model since it provides the best solutions for $Ra = 5.5 \times 10^5$. Figure 5a shows the model error for three central difference schemes of increasing accuracy. Most calculations performed for Galerkin projections employ the classical 2^{nd}-order finite difference scheme. As shown in the figure, this method has a poor performance even at early stages of the temporal integration. We also test 6^{th}- and 10^{th}-order compact schemes on the LSPG model. All calculations performed for the results presented earlier in the paper employ the latter scheme, which is shown to perform slightly better than the 6^{th}-order method, especially for long time-integration periods. Similar results were obtained for the Galerkin projection but are not shown. This aspect is rarely discussed but Galerkin models usually encountered in literature employ 2^{nd}-order schemes, typical of finite volume solvers. It is important to mention that flows involving a broad range of temporal and spatial scales require higher-order methods for accurate solutions.

Since the LSPG presents the best solutions for the present flow analyzed, we also investigate the influence of hyper-reduction on the accuracy of the model. The number of grid points used in the regression problem 21 must be previously chosen for this method, but there is no direct way to rigorously guarantee the parameter optimality or the error bounds a priori. Therefore, the weight of hyper-reduction stays as a free parameter that directly affects accuracy, computational

cost and numerical robustness. Figure 5b shows the evolution of the relative error for three LSPG models with increasing number of points. It is important to point out that the error does not decrease monotonically as the number of points is increased. This implies that the simple addition of more points in the model does not necessarily lead to a more accurate and robust ROM. However, it will certainly increase the cost. For the present case, we show that reducing the number of points in the hyper-reduction from $8\,574$ to $1\,413$ deteriorates the solution, leading to an increase in the relative error. Adding more points keeps the error low during early stages of the time integration but, for longer predictions, the solution obtained using $15\,668$ points produces larger errors than that computed using $8\,574$ nodes. Error prediction methods could possibly be used in the future as a decision mechanism for optimal selection of the number of nodes.

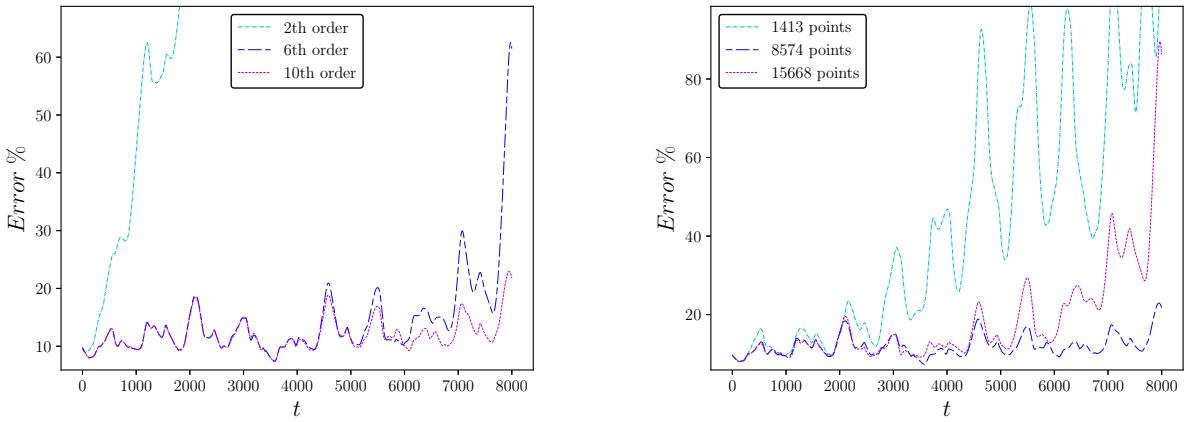

(a) Effects of scheme resolution.

(b) Effects of hyper-reduction.

Figure 5: Temporal evolution of relative error for $Ra = 5.5 \times 10^5$ using various finite difference schemes and different levels of hyper-reduction.

6. Preliminary Conclusions and Additions to the Final Paper

Despite the geometrical simplicity of the rectangular cavity, the current setup offers rich dynamics that depend on the thermal forcing. Hence, it is a suitable candidate to evaluate the performance of ROMs. In this work, we employ ROMs which are constructed based on time-accurate solutions of a full-order model (FOM) that solves the coupled Navier-Stokes and energy equations using a high-resolution spectral element method. Before the models are built , proper orthogonal decomposition (POD) is applied to reduce the problem dimensionality.

The classical Galerkin projection is tested as well as the least-squares Petrov-Galerkin (LSPG) method. This extended abstract shows a study for a moderate Rayleigh number flow that has non-periodic temporal dynamics. In order to accurately represent this flow, 14 POD modes are employed for the models. However, both the Galerkin and LSPG methods are built with 40 modes to maintain numerical stability but the last 26 modes are not used in the construction of the temperature and velocity fluctuation fields. It is shown that the POD modes for this case are composed of several frequencies which are excited in a non-periodical manner. The best results for this case are obtained with the LSPG.

In order to be cost effective, the LSPG approach depends on a hyper-reduction technique as discussed in the numerical methodology section. The weight of this hyper-reduction is a free parameter of the model that directly affects its accuracy, computational cost and robustness. We performed a study that shows the impact of different levels of hyper-reduction on the relative error of the model. We also demonstrate the importance of employing high-order numerical schemes for the calculation of spatial derivatives appearing in the models. In this context, for long time integration, the relative error of the temperature and velocity fluctuations remains much lower for a 10^{th}-order scheme than for a 2^{nd}-order one.

As a further step in the assessment of the ROM approaches presented here, higher-Ra cases will be considered, even though this would be very challenging for all models as broadband effects become dominant, thus requiring an often prohibitive number of spatial modes to recover all relevant flow features. In the final version of the paper, we will solve higher Ra number flows using a cluster POD approach. We will also discuss about the use of basis interpolation techniques to obtain ROM solutions for intermediate parameter values, or to construct ROMs which are valid for a range of parameters rather than for a single one.

Appendix: Galerkin Coefficients

Conside the Galerkin coefficients given by the following tensors $\mathbf{e}$, $\mathbf{A}$ and $\mathbf{N}$ from equation 19 and computational domain $\mathbf{\Omega}$. These coefficients are functions of the spatial basis $\mathbf{\Phi} = [\mathbf{\Phi_u}\ \mathbf{\Phi_v}\ \mathbf{\Phi_T}]^\top$ obtained by POD, mean field $\bar{\mathbf{q}} =$

$[\bar{\mathbf{u}}\ \bar{\mathbf{v}}\ \bar{\mathbf{T}}]^\top$ and initial conditions $[\mathbf{u_0}\ \mathbf{v_0}\ \mathbf{T_0}]^\top$.

It is convenient to decompose $\mathbf{e} = e_i = -e_i^1 - \sqrt{\frac{Pr}{Ra}} e_i^2 - \frac{1}{\sqrt{Pr\,Ra}} e_i^3 - e_i^4$, which leads to the following terms

$$\begin{aligned} e_i^1 = -\iint_\Omega \Bigg[& \boldsymbol{\Phi}_{\mathbf{u_i}} \left(\bar{\mathbf{u}} \frac{\partial \bar{\mathbf{u}}}{\partial x} + \bar{\mathbf{v}} \frac{\partial \bar{\mathbf{u}}}{\partial y} \right) + \\ & \boldsymbol{\Phi}_{\mathbf{v_i}} \left(\bar{\mathbf{u}} \frac{\partial \bar{\mathbf{v}}}{\partial x} + \bar{\mathbf{v}} \frac{\partial \bar{\mathbf{v}}}{\partial y} \right) + \\ & \boldsymbol{\Phi}_{\mathbf{T_i}} \left(\bar{\mathbf{u}} \frac{\partial \bar{\mathbf{T}}}{\partial x} + \bar{\mathbf{v}} \frac{\partial \bar{\mathbf{T}}}{\partial y} \right) \Bigg] \, dx\, dy \end{aligned} \tag{23}$$

$$e_i^2 = -\iint_\Omega \left(\frac{\partial \boldsymbol{\Phi}_{\mathbf{u_i}}}{\partial x} \frac{\partial \bar{\mathbf{u}}}{\partial x} + \frac{\partial \boldsymbol{\Phi}_{\mathbf{v_i}}}{\partial y} \frac{\partial \bar{\mathbf{v}}}{\partial y} \right) \, dx\, dy\,, \tag{24}$$

$$e_i^3 = -\iint_\Omega \left(\frac{\partial \boldsymbol{\Phi}_{\mathbf{T_i}}}{\partial x} \frac{\partial \bar{\mathbf{T}}}{\partial x} \right) \, dx\, dy\,, \tag{25}$$

and

$$e_i^4 = -\iint_\Omega \left(\boldsymbol{\Phi}_{\mathbf{v_i}} \bar{\mathbf{T}} \right) \, dx\, dy\,. \tag{26}$$

The term $\mathbf{A}$ is also conveniently decomposed as $\mathbf{A}$ as $A_{ij} = -A_{ij}^1 - \sqrt{\frac{Pr}{Ra}} A_{ij}^2 - \frac{1}{\sqrt{Pr\,Ra}} A_{ij}^3 - A_{ij}^4$

$$\begin{aligned} A_{ij}^1 = -\iint_\Omega \Bigg[& \boldsymbol{\Phi}_{\mathbf{u_i}} \left(\bar{\mathbf{u}} \frac{\partial \boldsymbol{\Phi}_{\mathbf{u_j}}}{\partial x} + \bar{\mathbf{v}} \frac{\partial \boldsymbol{\Phi}_{\mathbf{u_j}}}{\partial y} + \boldsymbol{\Phi}_{\mathbf{u_j}} \frac{\partial \bar{\mathbf{u}}}{\partial x} + \boldsymbol{\Phi}_{\mathbf{v_j}} \frac{\partial \bar{\mathbf{u}}}{\partial y} \right) + \\ & \boldsymbol{\Phi}_{\mathbf{v_i}} \left(\bar{\mathbf{u}} \frac{\partial \boldsymbol{\Phi}_{\mathbf{v_j}}}{\partial x} + \bar{\mathbf{v}} \frac{\partial \boldsymbol{\Phi}_{\mathbf{v_j}}}{\partial y} + \boldsymbol{\Phi}_{\mathbf{u_j}} \frac{\partial \bar{\mathbf{v}}}{\partial x} + \boldsymbol{\Phi}_{\mathbf{v_j}} \frac{\partial \bar{\mathbf{v}}}{\partial y} \right) + \\ & \boldsymbol{\Phi}_{\mathbf{T_i}} \left(\bar{\mathbf{u}} \frac{\partial \boldsymbol{\Phi}_{\mathbf{T_j}}}{\partial x} + \bar{\mathbf{v}} \frac{\partial \boldsymbol{\Phi}_{\mathbf{T_j}}}{\partial y} + \boldsymbol{\Phi}_{\mathbf{u_j}} \frac{\partial \bar{\mathbf{T}}}{\partial x} + \boldsymbol{\Phi}_{\mathbf{v_j}} \frac{\partial \bar{\mathbf{T}}}{\partial y} \right) \Bigg] \, dx\, dy \end{aligned} \tag{27}$$

$$\begin{aligned} A_{ij}^2 = -\iint_\Omega \Bigg(& \frac{\partial \boldsymbol{\Phi}_{\mathbf{u_i}}}{\partial x} \frac{\partial \boldsymbol{\Phi}_{\mathbf{u_j}}}{\partial x} + \frac{\partial \boldsymbol{\Phi}_{\mathbf{u_i}}}{\partial y} \frac{\partial \boldsymbol{\Phi}_{\mathbf{u_j}}}{\partial y} + \\ & \frac{\partial \boldsymbol{\Phi}_{\mathbf{v_i}}}{\partial x} \frac{\partial \boldsymbol{\Phi}_{\mathbf{v_j}}}{\partial x} + \frac{\partial \boldsymbol{\Phi}_{\mathbf{v_i}}}{\partial y} \frac{\partial \boldsymbol{\Phi}_{\mathbf{v_j}}}{\partial y} \Bigg) \, dx\, dy\,, \end{aligned} \tag{28}$$

$$A_{ij}^3 = -\iint_\Omega \left(\frac{\partial \boldsymbol{\Phi}_{\mathbf{T_i}}}{\partial x} \frac{\partial \boldsymbol{\Phi}_{\mathbf{T_j}}}{\partial x} + \frac{\partial \boldsymbol{\Phi}_{\mathbf{T_i}}}{\partial y} \frac{\partial \boldsymbol{\Phi}_{\mathbf{T_j}}}{\partial y} \right) \, dx\, dy\,, \tag{29}$$

$$A_{ij}^4 = -\iint_\Omega \left(\boldsymbol{\Phi}_{\mathbf{v_i}} \boldsymbol{\Phi}_{\mathbf{T_j}} \right) \, dx\, dy\,, \tag{30}$$

and, finally, the third order tensor is written as

$$\begin{aligned} N_{ijk} = -\iint_\Omega \Bigg[& \boldsymbol{\Phi}_{\mathbf{u_i}} \left(\boldsymbol{\Phi}_{\mathbf{u_j}} \frac{\partial \boldsymbol{\Phi}_{\mathbf{u_k}}}{\partial x} + \boldsymbol{\Phi}_{\mathbf{v_j}} \frac{\partial \boldsymbol{\Phi}_{\mathbf{u_k}}}{\partial y} \right) + \\ & \boldsymbol{\Phi}_{\mathbf{v_i}} \left(\boldsymbol{\Phi}_{\mathbf{u_j}} \frac{\partial \boldsymbol{\Phi}_{\mathbf{v_k}}}{\partial x} + \boldsymbol{\Phi}_{\mathbf{v_j}} \frac{\partial \boldsymbol{\Phi}_{\mathbf{v_k}}}{\partial y} \right) + \\ & \boldsymbol{\Phi}_{\mathbf{T_i}} \left(\boldsymbol{\Phi}_{\mathbf{u_j}} \frac{\partial \boldsymbol{\Phi}_{\mathbf{T_k}}}{\partial x} + \boldsymbol{\Phi}_{\mathbf{v_j}} \frac{\partial \boldsymbol{\Phi}_{\mathbf{T_k}}}{\partial y} \right) \Bigg] \, dx\, dy\,. \end{aligned} \tag{31}$$

The initial condition of 19 is obtained by projection of the first snapshot on the basis vector as

$$a_i(0) = \iint_\Omega \left((\mathbf{u_0} - \bar{\mathbf{u}}) \boldsymbol{\Phi}_{\mathbf{u_i}} + (\mathbf{v_0} - \bar{\mathbf{v}}) \boldsymbol{\Phi}_{\mathbf{v_i}} + (\mathbf{T_0} - \bar{\mathbf{T}}) \boldsymbol{\Phi}_{\mathbf{T_i}} \right) \, dx\, dy\,. \tag{32}$$

Acknowledgments

The authors of this work would like to acknowledge Fundação de Amparo à Pesquisa do Estado de São Paulo, FAPESP, for supporting the present work under research grants No. 2013/08293-7, 2018/11410-9 and 2019/18809-7.

7. REFERENCES

A Quarteroni, A.M. and Negri, F., 2016. *Reduced Basis Methods for Partial Differential Equations: An Introduction*. Springer, Switzerland, 1st edition.

Amsallem, D., Zahr, M.J. and Farhat, C., 2012. "Nonlinear model order reduction based on local reduced-order bases". *International Journal for Numerical Methods in Engineering*, Vol. 92, pp. 891–916. doi:10.1002/nme.4371.

Astrid, P., Weiland, S., Willcox, K. and Backx, T., 2008. "Missing point estimation in models described by proper orthogonal decomposition". *IEEE Transactions on Automatic Control*, Vol. 53, pp. 2237–2251. doi: 10.1109/TAC.2008.2006102.

Balajewicz, M., Tezaur, I. and Dowell, E., 2016. "Minimal subspace rotation on the Stiefel manifold for stabilization and enhancement of projection-based reduced order models for the compressible Navier-Stokes equations". *Journal of Computational Physics*, Vol. 321, pp. 224–241. ISSN 0021-9991. doi:http://dx.doi.org/10.1016/j.jcp.2016.05.037. URL `http://www.sciencedirect.com/science/article/pii/S0021999116301826`.

Bergmann, M., Cordier, L. and Brancher, J.P., 2005. "Optimal rotary control of the cylinder wake using proper orthogonal decomposition reduced-order model". *Physics of Fluids*, Vol. 17, p. 097101. doi:10.1063/1.2033624.

Bergmann, M., Ferrero, A., Iollo, A., Lombardi, E., Scardigli, A. and Telib, H., 2018. "A zonal galerkin-free pod model for incompressible flows". *Journal of Computational Physics*, Vol. 352, pp. 301–325.

Blackburn, H.M. and Sherwin, S., 2004. "Formulation of a Galerkin spectral element–Fourier method for three-dimensional incompressible flows in cylindrical geometries". *Journal of Computational Physics*, Vol. 197, No. 2, pp. 759–778.

Carlberg, K., Barone, M. and Antil, H., 2017. "Galerkin v. least-squares Petrov-Galerkin projection in nonlinear model reduction". *Journal of Computational Physics*, Vol. 330, pp. 693–734. doi:10.1016/j.jcp.2016.10.033.

Carlberg, K., Farhat, C. and Amsallem, D., 2013. "The GNAT method for nonlinear model reduction: Effective implementation and application to computational fluid dynamics and tubulent flows". *Journal of Computational Physics*, Vol. 243, pp. 623–647. doi:10.1016/j.jcp.2013.02.028.

Cazemier, W., Verstappen, R.W.C.P. and Veldman, A.E.P., 1998. "Proper orthogonal decomposition and low-dimensional models for driven cavity flows". *Physics of Fluids*, Vol. 10, No. 7, pp. 1685–1699. doi:10.1063/1.869686.

Chaturantabut, S. and Sorensen, D.C., 2010. "Nonlinear model reduction via discrete empirical interpolation". *SIAM Journal on Scientific Computing*, Vol. 32, pp. 2737–3764. doi:10.1137/090766498.

Christon, M.A., Gresho, P.M. and Sutton, S.B., 2002. "Computational predictability of time-dependent natural convection flows in enclosures (including a benchmark solution)". *International Journal for Numerical Methods in Fluids*, Vol. 40, No. 8, pp. 953–980.

Cordier, L. and Bergmann, M., 2008. "Proper Orthogonal Decomposition: an overview". In *Lecture series 2002-04, 2003-03 and 2008-01 on post-processing of experimental and numerical data, Von Karman Institute for Fluid Dynamics, 2008.*, VKI, p. 46 pages. URL `https://hal.archives-ouvertes.fr/hal-00417819`.

Everson, R. and Sirovich, L., 1995. "Karhunun-loève procedure for gappy data". *Optical Society of America*, Vol. 12, pp. 1657–1664. doi:10.1364/JOSAA.12.001657.

Gjesdal, T., Wasberg, C.E. and Reif, B.A.P., 2006. "Spectral element benchmark simulations of natural convection in two-dimensional cavities". *International journal for numerical methods in fluids*, Vol. 50, No. 11, pp. 1297–1319.

Karniadakis, G. and Sherwin, S., 2013. *Spectral/hp element methods for computational fluid dynamics*. Oxford University Press.

Karniadakis, G.E., Israeli, M. and Orszag, S.A., 1991. "High-order splitting methods for the incompressible Navier-Stokes equations". *Journal of Computational Physics*, Vol. 97, No. 2, pp. 414–443.

Östh, J., Noack, B.R., Krajnović, S., Barros, D. and Borée, J., 2014. "On the need for a nonlinear subscale turbulence term in POD models as exemplified for a high-Reynolds-number flow over an Ahmed body". *Journal of Fluid Mechanics*, Vol. 747, pp. 518–544. doi:10.1017/jfm.2014.168.

Protas, B., Noack, B.R. and Östh, J., 2015. "Optimal nonlinear eddy viscosity in Galerkin models of turbulent flows". *Journal of Fluid Mechanics*, Vol. 766, pp. 337–367. doi:10.1017/jfm.2015.14.

Rowley, C.W., Colonius, T. and Murray, R.M., 2004. "Model reduction for compressible flows using POD and galerkin projection". *Physica D: Nonlinear Phenomena*, Vol. 189, No. 1–2, pp. 115 – 129.

San, O. and Maulik, R., 2018a. "Extreme learning machine for reduced order modeling of turbulent geophysical flows". *Phys. Rev. E*, Vol. 97, p. 042322. doi:10.1103/PhysRevE.97.042322. URL `https://link.aps.org/doi/10.1103/PhysRevE.97.042322`.

San, O. and Maulik, R., 2018b. "Machine learning closures for model order reduction of thermal fluids". *Applied Mathematical Modelling*, Vol. 60, pp. 681–710.

Sirovich, L., 1987. "Turbulence and the dynamics of coherent structures. Part 1: Coherent structures". *Quarterly of Applied Mathematics*, Vol. 45, pp. 561–571. doi:10.1090/qam/910463.

Willcox, K., 2006. "Unsteady flow sensing and estimation via the gappy proper orthogonal decomposition". *Computers*

& Fluids, Vol. 35, pp. 208–226. doi:10.1016/j.compfluid.2004.11.006.

Xin, S. and Quere, P.L., 2002. "An extended chebyshev pseudo-spectral benchmark for the 8: 1 differentially heated cavity". *International Journal for Numerical Methods in Fluids*, Vol. 40, No. 8, pp. 981–998.

Zimmermann, R. and Willcox, K., 2016. "An accelerated greedy missing point estimation procedure". *SIAM Journal on Scientific Computing*, Vol. 38, pp. A2827–A2850. doi:10.1137/15M1042899.

8. RESPONSIBILITY NOTICE

The following text, properly adapted to the number of authors, must be included in the last section of the paper: The author(s) is (are) solely responsible for the printed material included in this paper.